# Soft Matter

Accepted Manuscript


This is an *Accepted Manuscript*, which has been through the Royal Society of Chemistry peer review process and has been accepted for publication.

*Accepted Manuscripts* are published online shortly after acceptance, before technical editing, formatting and proof reading. Using this free service, authors can make their results available to the community, in citable form, before we publish the edited article. We will replace this *Accepted Manuscript* with the edited and formatted *Advance Article* as soon as it is available.

You can find more information about *Accepted Manuscripts* in the Information for Authors.

Please note that technical editing may introduce minor changes to the text and/or graphics, which may alter content. The journal's standard Terms & Conditions and the Ethical guidelines still apply. In no event shall the Royal Society of Chemistry be held responsible for any errors or omissions in this *Accepted Manuscript* or any consequences arising from the use of any information it contains.

ROYAL SOCIETY OF CHEMISTRY

www.rsc.org/softmatter

Journal Name

ARTICLE TYPE

Cite this: DOI: 10.1039/xxxxxxxxxx

# Deformation of a soft helical filament in an axial flow at low Reynolds number†

Mohammad K. Jawed,[a] and Pedro M. Reis*[ab]

Received Date
Accepted Date

DOI: 10.1039/xxxxxxxxxx

www.rsc.org/journalname

We perform a numerical investigation of the deformation of a rotating helical filament subjected to an axial flow, under low Reynolds number conditions, motivated by the propulsion of bacteria using helical flagella. Given its slenderness, the helical rod is intrinsically soft and deforms due to the interplay between elastic forces and hydrodynamic loading. We make use of a previously developed and experimentally validated computational tool that models the elasticity of the filament using the Discrete Elastic Rod method and the fluid forces are treated using Lighthill's Slender Body Theory. Under axial flow, and in the absence of rotation, the initially helical rod is extended. Above a critical flow speed its configuration comprises a straight portion connected to a localized helix near the free end. When the rod is also rotated about its helical axis, propulsion is only possible in a finite range of angular velocity, with an upper bound that is limited by buckling of the soft helix arising due to viscous stresses. A systematic exploration of the parameter space allows us to quantify regimes for successful propulsion for a number of specific bacteria.

## 1 Introduction

Slender helical rods under hydrodynamic loading may undergo geometrically nonlinear deformation; a canonical example of which is the flagellum of a bacterium. The rotation of one or more of these rod-like helical structures generates a propulsive force that enables the translation of bacteria [1]. At the microscopic scale of flagella, viscous loading generated by the fluid dominates over inertia, and flagellar propulsion occurs in the low Reynolds number or *Stokes* regime [1]. The combined effect of the hydrodynamic forces on flagella arising from the viscous medium coupled with their slenderness-induced flexibility (or *softness*) can result in geometrically nonlinear deformed configurations [2–5]. Moreover, the deformation of a flagellum under axial flow has enabled measurements of its bending rigidity [6] and has allowed for the probing of the controlled transformation between different polymorphic forms [7]. This experimental work has motivated a series of computational studies that have numerically analyzed the observed modes of deformation [8,9]. However, these simulation efforts either used Resistive Force Theory [10,11], which cannot yield quantitative agreement with experiments [12], or considered linear deflections, thereby overlooking the geometrically-nonlinear deformations. The importance of these nonlinearities has indeed been highlighted by the synthesis of microscale helical ribbons and the quantification of their modes of deformation under axial flow [13]. Motivated by this context of natural and artificial flagella, we have recently combined precision model experiments with numerical simulations to study the propulsion of a soft filament rotating about its helical axis, clamped at one end fixed in space [14]. Beyond a critical angular rotation speed, we found that the hydrodynamic forces can cause the filament to buckle and exhibit strong geometric-nonlinearities. This threshold was found to be approximately within one order of magnitude of the operating angular speed during locomotion of some well-studied bacteria. Inspired by these results, we now place emphasis on the effect of axial flow on this instability mechanism and its effect on propulsion.

Here, we perform a systematic numerical investigation of a rotating helical filament deformed by an axial flow (see Fig. 1), under low Reynolds number conditions. Our goal is to establish a description for the configurations that ensue. Our system is inspired by the dynamics of a bacterial flagellum, but, for simplicity and to avoid loss of generality, we have decided not to consider the hydrodynamic effects of the cell body. We consider the combined effect of rotation and translation of the flow with respect to the filament to quantify the resulting propulsive force, as well as characterize the underlying mechanical instabilities. Our numerical model couples the Discrete Elastic Rod (DER) method [15–17] for a geometric-nonlinear elastic description of the slender filament, with Lighthill's Slender Body Theory (LSBT) [10] to account for the important long-range hydrodynamic interactions between distant portions of the filament.

[a] Department of Mechanical Engineering, Massachusetts Institute of Technology, Cambridge, MA, USA 02139
[b] Department of Civil and Environmental Engineering, Massachusetts Institute of Technology, Cambridge, MA, USA 02139

Exploiting the robustness and efficiency of our computational approach, we first map out the elongation of the initially helical rod as a function of the axial flow speed, our primary control parameter, and the other relevant geometric, material, and fluid properties. Motivated by the swimming (translation) of uniflagellated bacteria through their rotating flagellum, our exploration is then extended to include a rotating helical rod under axial flow. We evaluate the minimum and maximum angular rotation velocity for successful propulsion in our reduced model setting. These two bounds coalesce at a critical axial flow speed, such that propulsion is not feasible beyond this threshold. We then survey this limiting range for biologically relevant parameters to assess their pertinence to propulsion.

## 2 Definition of the problem

We consider a linear elastic rod with a right-handed helical configuration in its stress-free state (axial length, $l$, pitch, $\lambda$, and helix pitch, $R$; see Fig. 1d). Its cross-section is circular with radius, $r_0 \ll l$, such that the area moment of inertia is $I = \pi r_0^4/4$. The rod is immersed in a viscous fluid with dynamic viscosity $\mu$ and density $\rho$. One end of the helical rod is clamped and translated along the negative direction of the $x$-axis (see Fig. 1d for details on the coordinate system), that is equivalent to imposing a uniform flow with speed, $v$, aligned along the positive $x$-axis, as long as the Reynolds number remains $Re = vr_0\rho/\mu \ll 1$. An angular velocity, $\omega$, is also prescribed to the clamped end. The sign of $\omega$ is taken to be positive, if the clamp rotates in the anti-clockwise direction, when the helix is seen from above. The other extremity of the rod is set free. To aim for generality of the results and for simplicity, throughout our study in a model setting we do not consider an equivalent of the cell body. Therefore, when connections are established with the original biological system, we neglect the hydrodynamic interaction between the cell body and the flagellum, although this is an effect that should be considered in future studies. It is also important to note that, in natural bacterial propulsion, the net force and torque generated by the flagella are canceled by the opposite force and torque from the cell body, and thus result in a force-free and torque-free system. In our system, since the filament is rotated at a clamped point that is fixed in space, for any net force generated by the helical filament, there is an equal and opposite reaction force at the clamp.

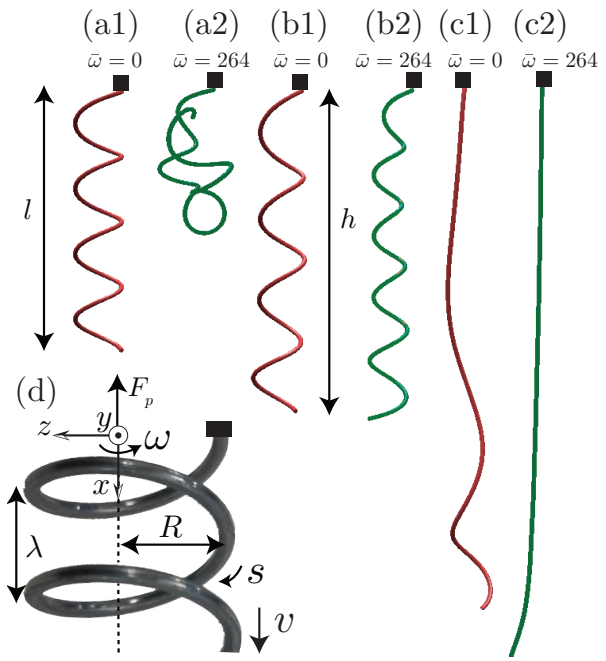


**Fig. 1** Representative configurations of a soft helix subjected to an axial flow (aligned vertically, from top to bottom): (a) undeformed helix ($\bar{v} = 0$), (b) stretched helix ($\bar{v} = 10.5$), and (c) localized helix ($\bar{v} = 105$). The clamped end (black square) is rotated with the dimensionless angular velocity of $\bar{\omega} = 0$ shown in red in (a1), (b1), (c1) and $\bar{\omega} = 264$ shown in green in (a2), (b2), (c2). The physical parameters correspond to the representative case detailed in the text. The configurations were recorded at the dimensionless time $\bar{t} = 0.71$. (d) Schematic diagram showing the relevant geometric quantities.

All the numerical experiments in this paper employ a *representative rod* that has a normalized pitch, $\lambda/l = 0.25$, and normalized radius, $R/\lambda = 0.318$, unless stated otherwise. This choice is such that these geometric parameters lie in the respective known ranges of bacterial flagella [12,18]: $0.1 \lesssim \lambda/l \lesssim 0.4$ and $0.07 \lesssim R/\lambda \lesssim 0.4$. A characteristic velocity $EI/[\mu l^3]$ can be constructed from the balance of viscous and elastic effects ($EI$ is the bending stiffness of the rod), and is used throughout to normalize the axial velocity as $\bar{v} = v\mu l^3/[EI]$. This nondimensionalization scheme is verified in detail in §4, below. Our focus is to span the regimes where elasticity dominates ($\bar{v} \ll 1$) and where viscous loading is prevalent ($\bar{v} \gg 1$), and capture the coupling that leads to mechanical instabilities of the filament in the cross-over region at $v \sim EI/[\mu l^3]$. Existing comparisons between this scenario and the natural systems have underlined the importance of this interplay [14]. Similarly, the characteristic frequency obtained from the balance of bending forces and viscous drag is used to nondimensionalize the angular rotation speed (imposed at the clamp) as $\bar{\omega} = \omega\mu l^4/[EI]$ and time as $\bar{t} = tEI/[\mu l^4]$ [14]. The specific dimensional physical properties used in our simulations are provided in §3.

In Figs. 1a-c, we present a series of representative configurations of deformed helices in steady state at three different values of the axial flow speed. In the absence of rotation (Figs. 1a1,b1,c1 for $\bar{\omega} = 0$), the rod assumes a helical configuration which, for high enough values of $\bar{v}$, may be localized (near the clamp, the rod has a straight portion that is connected to a helix near the tip). When the angular velocity is nonzero (Figs. 1a2,b2,c2), the rod can buckle (Fig. 1a2), or the presence of a nonzero axial flow may prevent buckling from occurring (Fig. 1b2, c2).

To systematically quantify the deformation process, the suspended height, $h$ (vertical distance along the helix axis between the clamp and the tip of the rod), is taken as a shape parameter. We shall start by first addressing the elongation of a helix under axial flow with $\bar{\omega} = 0$, and provide a general description. We will then account for the rotation of the helix, which generates a normalized propulsive force, $\bar{F}_p = F_p l^2/[EI]$, and can induce buckling in the rod if a critical angular velocity, $\bar{\omega}_b$, is reached; a typical buckled configuration is presented in Fig. 1(a). These two quantities, $\bar{\omega}_b$ and $\bar{F}_p$, are evaluated for a few representative model helices that are geometrically similar to some well-known bacterial flagella. At a given flow speed, $\bar{v}$, this allows us to estab-

lish boundaries for minimum angular velocity necessary to sustain propulsion, and the maximum angular velocity above which buckling takes place. Furthermore, if the flow speed, $\bar{v}$, is too high, buckling may occur even before the minimum value of $\bar{\omega}$ to sustain propulsion ($\bar{F}_p > 0$) is reached. This sets an upper bound on the axial speed, which we quantify for our helical filaments.

## 3 Numerical simulation approach

The numerical tool used to study the fluid-structure interaction problem described above combines: i) the Discrete Elastic Rod (DER) method[16] to simulate the elasticity of the structure, and ii) Lighthill's Slender Body Theory (LSBT)[10] for a long range hydrodynamic force model for the viscous medium. Both DER and LSBT have been independently validated in detail against precision experiments[12,19], and likewise for the aforesaid coupled implementation[14]. A detailed account for the formulation that couples DER with LSBT, as well as boundary conditions, is provided in Ref.[14].

The DER method[16] represents a Kirchhoff elastic rod[20] by the centerline, $\gamma(s)$, and its angular evolution, $\theta(s)$, both of which are parameterized by the arc-length, $s$. The strains in a deformed rod can then be computed from the twist, $\theta'(s)$, curvature, $|\gamma''(s)|$, and axial stretching.

The relation between the velocity, $\mathbf{u}(s)$, and the viscous force per unit length, $\mathbf{f}(s)$, is provided by LSBT as

$$\mathbf{u}(s) = \frac{1}{8\pi\mu}\left(2\mathbf{f}(s)\cdot(\mathbb{I}-\mathbf{t}(s)\otimes\mathbf{t}(s)) + \int \mathbf{f}(s')\cdot\left(\frac{\mathbb{I}}{|\mathbf{r}|}+\frac{\mathbf{r}\otimes\mathbf{r}}{|\mathbf{r}|^3}\right)\mathrm{d}s'\right), \tag{1}$$

where $\mathbf{t}(s)$ is tangent to the centerline and $\mathbf{r} = \mathbf{r}(s) - \mathbf{r}(s')$ is the position vector of a point at $s$, with respect to another at $s'$. The integration is performed over $|\mathbf{r}| > r_0\sqrt{e}/2$, where $r_0$ is the cross-sectional radius of the rod, and the quantity $r_0\sqrt{e}/2$ is referred to as the cut-off length[10]. The propulsive force on the clamping point that results from the rotation of the helical filament can be calculated by integrating the viscous force along the arc-length, $F_p = -\int_0^L \mathbf{f}\cdot\mathbf{e}_x \mathrm{d}s$, where $L$ is the contour length of the helix. In the discrete setting, the rod is composed of a collection of $N$ nodes along the centerline. For the representative case we set $N = 173$, such that the distance between nodes is twice the cut-off length $r_0\sqrt{e}/2$ in Eq. (1). At each time step in DER, LSBT is used through Eq. (1) to relate the velocity at each node with the viscous forces applied by the fluid on all the nodes. The positions of the first two nodes on the rod are constrained such that the helix axis at the clamp is always aligned along $\mathbf{e}_x$.

Unless noted otherwise, the rod in our numerical experiments has a Young's modulus $E = 1255\,\mathrm{kPa}$, Poisson ratio $\nu = 0.5$ (*i.e.*, incompressible material), and an axial length $l = 0.2\,\mathrm{m}$. The ratio of length to cross-sectional radius is $r_0/l = 126$. The density of the rod, $\rho_r = 1.273\ \mathrm{g/cm^3}$, is equal to the density of the viscous medium, such that buoyancy can be neglected. The viscosity of the fluid medium is $\mu = 1.6\ \mathrm{Pa\cdot s}$. These parameters are identical to the experiments reported in Ref.[14]. Hereafter, we shall refer to simulations with the above set of parameters as the *representative case*. To ensure generality of our results and applicability across length scales, our simulations results are presented throughout in a dimensionless form using the nondimensionalization scheme introduced in §2, above.

## 4 Deformation under axial flow

We start our investigation by quantifying the deformation of a helix under a uniform axial flow in the $\mathbf{e}_x$ direction, along the axis of the helix, and sweep the relevant physical parameters. Our goal is to obtain a generic description of the suspended height as a function of the relevant physical parameters. Throughout this section, the helical filament is *not* rotated, *i.e.*, the angular velocity is fixed at $\bar{\omega} = 0$.

In Fig. 2, we present time series of the dimensionless suspended height of the rod, $\bar{h} = h/l$ (normalized by the initial axial length, $l$) for two instances of identical magnitude of the flow speed, but opposite directions: $\bar{v} = 105$ (solid line) and $\bar{v} = -105$ (dashed line), respectively. In both cases, the initial time evolution of the suspended height is approximately linear, up to $\bar{t} \lesssim 10^{-2}$, albeit with opposite slopes as the helix is moderately extended or compressed, respectively (see inset of Fig. 2). Eventually, both cases asymptote to steady values. For $\bar{v} = 105$, past the initial linear regime, $\bar{h}$ reaches the steady state height of $\bar{h} = 1.99$ (see Fig. 2b1-b4 for the corresponding sequence of configurations). By contrast, for $\bar{v} = -105$ (see Fig. 2c1-c4), $\bar{h}$ decreases with time and eventually reaches a steady state configuration that appears as a flipped version of the case above with positive axial speed. When $\bar{t} \lesssim 10^{-2}$ (Fig. 2c1), the helix compression is approximately linear with time, and then undergoes a sudden shape change at $\bar{t} \approx 10^{-2}$ (Fig. 2c2) when the free end of the helix bypasses the clamped end (Fig. 2c3). At this point, $\bar{h}$ becomes negative and eventually reaches $\bar{h} = 1.92$ (Fig. 2c4). The primary difference between the $\bar{v} = 105$ and $\bar{v} = -105$ cases is the imposed angle between the helix axis at the clamp and the direction of the flow velocity. This results in a slightly higher steady state value of the former ($\bar{h} = 1.99$), compared to the latter ($\bar{h} = 1.92$), due to the boundary layer of the rod near the clamp for the second case.

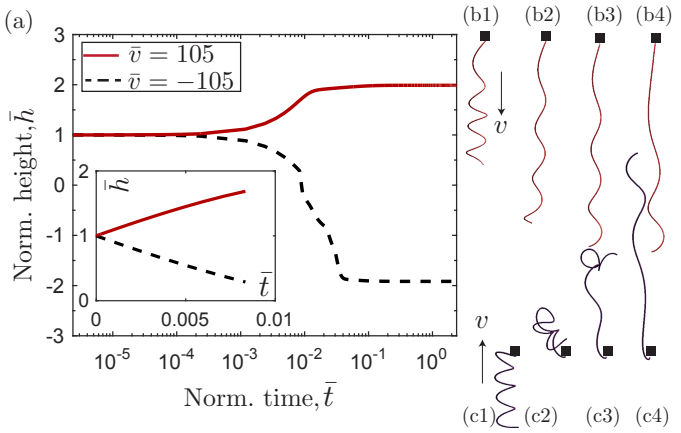


**Fig. 2** (a) Time series of normalized suspended height, $\bar{h}$, of the representative rod at $\bar{v} = 105$ cm/s (solid line) and $\bar{v} = -105$ (dashed line). Inset: Zoomed in region of the plot shows a linear relation between $\bar{h}$ and $\bar{t}$ near $\bar{t} = 0$. Time series of representative configurations for (b) $\bar{v} = 105$ and (c) $\bar{v} = -105$ at (b1, c1) $\bar{t} = 0.0024$, (b2, c2) $\bar{t} = 0.011$, (b3, c3)$\bar{t} = 0.024$, and (b4, c4) $\bar{t} = 0.238$.

From here on, we focus on analyzing the steady state values of the suspended height of the helical filament as a measure of its deformation, for a variety of parameters and flow configurations.

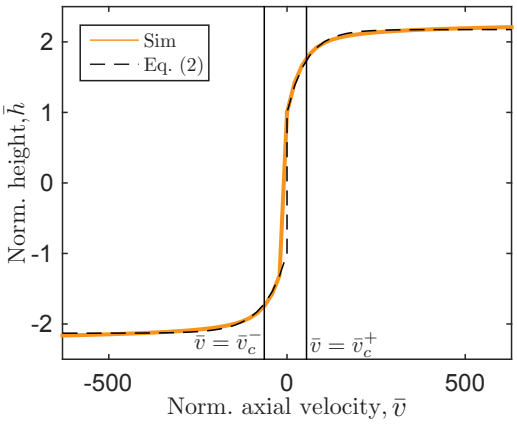


**Fig. 3** Normalized suspended height, $\bar{h}$, in steady state as a function of axial speed, $v$, for the representative rod. The dashed line is a fit to Eq. (2) with the parameters: $C^+ = 1.18 \pm 0.01$ and $\bar{v}_c^+ = 55 \pm 3$ for $\bar{v} \geq 0$; $C^- = 1.13 \pm 0.01$ and $v_c^- = 64 \pm 4$ for $\bar{v} < 0$.

In Fig. 3, we plot the steady state value of the normalized suspended height $\bar{h}$ as a function of the axial flow velocity. First, when the axial flow is oriented along the $\mathbf{e}_x$ ($\bar{v} > 0$), we find that the suspended height increases monotonically with $\bar{v}$ and eventually asymptotes to $\bar{h} \approx 2$. For characterization purposes, we describe this $\bar{h}(v)$ curve heuristically as

$$\bar{h} = \delta \left[ 1 + C \left( 1 - e^{-\delta v / v_c} \right) \right], \tag{2}$$

where both $C$ and $v_c$ are fitting parameters and $\delta$ can be either -1 or 1, for $\bar{v} < 0$ or $\bar{v} \geq 0$, respectively. Note that $C$ and $v_c$ can have slightly different values for $\bar{v} < 0$ (or $\bar{v} \geq 0$), which we shall distinguish by $C^-$ (or $C^+$) and $\bar{v}^-$ (or $\bar{v}^+$). The fit of the data to Eq. (2) is represented by a dashed line in Fig. 3a. The parameter $v_c$ (vertical solid lines in Fig. 3a) is hereafter referred to as the *characteristic speed* and delineates the *stretched helix* regime ($|\bar{v}| < \bar{v}_c$, Fig. 1b1) and the *localized helix* regime ($|\bar{v}| > \bar{v}_c$, Fig. 1c1). The parameter $C$ provides an estimate of elongation when $\bar{v}$ approaches infinity, and is termed the *elongation parameter*. Since the tip of the filament is free of moments, the helical rod never reaches a completely straight configuration. On the other hand, when the axial flow is set along the $-\mathbf{e}_x$ direction (*i.e.*, from free end towards the clamped end) so that $\bar{v} < 0$, the steady state suspended height, $\bar{h}$, decreases and the helix flips over to reach $\bar{h} = -1$ at $\bar{v} \approx -20$. Beyond that point, the height can also be described by Eq. (2) with $\delta = -1$. Fitting the data for $\bar{v} < 0$ yields $C^- = 1.13 \pm 0.01$ (vs. $C^+ = 1.18 \pm 0.01$ for $\bar{v} \geq 0$) and $\bar{v}_c^- = 63.8 \pm 3.5$ (vs. $\bar{v}_c^+ = 54.7 \pm 3.4$ for $\bar{v} \geq 0$). The slight mismatch between $C^+$ and $C^-$, as well as $\bar{v}_c^+$ and $\bar{v}_c^-$ can be attributed to the boundary condition at the clamped end: unlike the case of positive axial speed, the helix exits the clamp in the direction opposite to $\bar{v}$ when $\bar{v} < 0$. Hereafter, all the measurements of $C$ and $\bar{v}_C$ correspond to $C^+$ and $\bar{v}_c^+$, respectively.

It is worth mentioning that there is a direct analogy between the deformation of our helical filaments due to axial flow and the shapes of suspended curly hair[21]. For this later case, the deformation of a suspended naturally curved rod under gravity exhibits three qualitatively distinct configuration regimes – planar curls, localized helices, and global helices – each of which has well-defined phase boundaries. In the present study, the viscous drag induced by the axial flow plays a role similar to that of gravity in the aforementioned problem.

Having described the behavior of $\bar{h}(v)$ for a specific helical filament, we now seek to explore the parameter space by quantifying the characteristic speed, $v_c$, for a range of other geometric $(l, \lambda, R)$, material $(E, I)$, and fluid $(\mu)$ parameters. The radius of the filament, $r_0$, has been found to have a negligible effect on the flow[14] (confirmed again below) and is therefore not considered as a parameter in the fluid description. The steady state shape of the rod is set by a balance between the external viscous drag forces and the internal elastic forces. The rod can be treated as inextensible due to its slenderness such that elastic forces arise due to bending. Balancing the characteristic forces per unit length for bending, $f_b \sim EI/l^2$, and viscous drag, $f_v \sim \mu v l$, yields a scaling law for the characteristic flow speed

$$v_c \sim \frac{EI}{\mu l^3}, \tag{3}$$

for a fixed set of geometric parameters. Moreover, $R/\lambda$ and $\lambda/l$ are chosen to be the dimensionless groups representing the helical geometry. Note that the torsional stiffness is directly proportional to the bending stiffness of an incompressible rod, and therefore, a balance between viscous and twisting forces would have given the same scaling law.

In Fig. 4a, we plot $v_c$ as a function of $EI/[\mu l^3]$ obtained from a series of simulations in the range of $0 < \bar{v} \lesssim 10^4$, following a procedure similar to that used in Fig. 3. Starting from the parameters of the representative case (see §3), each of the relevant parameters, $\{E, r_0, l, \mu\}$, are independently and individually varied, while fixing the geometric groups $R/\lambda = 0.318$ and $\lambda/l = 0.25$. We find that all the data collapse onto a master curve that agrees well with the scaling in Eq. (3) (solid line in Fig. 4). It is therefore appropriate to nondimensionalize the characteristic speed as $\bar{v}_c = v_c \mu l^3/[EI]$. To estimate the value of $v_c$ for bacterial flagella, we extrapolate this scaling to obtain $EI/[\mu l^3] = 10^{-5}$ m/s (represented by the vertical dashed line in Fig. 4), for which we used an order of magnitude estimates of ($EI \sim 10^{-23}$ N/m$^2$)[22], ($\mu = 10^{-3}$ Pa.s), and ($l \sim 10^{-5}$ m)[12]. Our data in Fig. 4 indicates that the critical velocity in bacterial regime is $v_c = 4.27 \cdot 10^{-4}$ m/s. For the data presented in Fig. 4, the normalized axial force at $v = v_c$ exerted on the filament by the fluid is $-\bar{F}_p = 148 \pm 10$. Results reported previously[7] for the force versus extension with real bacterial flagella (also see numerical investigation in Ref.[8]) show significant change in shape at this force level that eventually leads to the triggering of a polymorphic transformation at normalized forces of $\sim 10^2$. The fact that the both of this force values is of the same order of magnitude is intriguing but a detailed study of polymorphism is beyond the scope of our study.

In Fig. 4b, we plot the elongation parameter, $C$, used in Eq. (2), as a function of $EI/[\mu l^3]$, for the same set of data used in Fig. 4a.

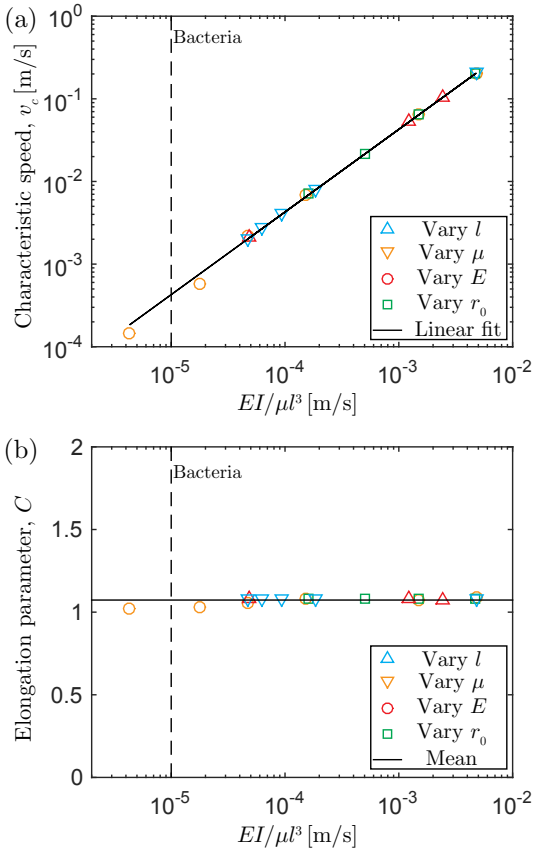


**Fig. 4** (a) Critical speed, $v_c$, as a function of characteristic speed, $EI/[\mu l^3]$. The parameter sweep starts with the parameters of the *representative* rod, and while keeping three of the four parameters $\{E, r_0, \mu, l\}$ fixed, the forth is varied. The geometric parameters, $\lambda/l$ and $R/\lambda$, are kept constant. The data can be best fitted by $v_c = (42.7 \pm 0.3) EI/[\mu l^3]$ (solid line). (b) The elongation parameter, $C$, in Eq. (3) is obtained from the same set of data. The solid line represents the mean, $C = 1.07$, that has a standard deviation of 0.01.

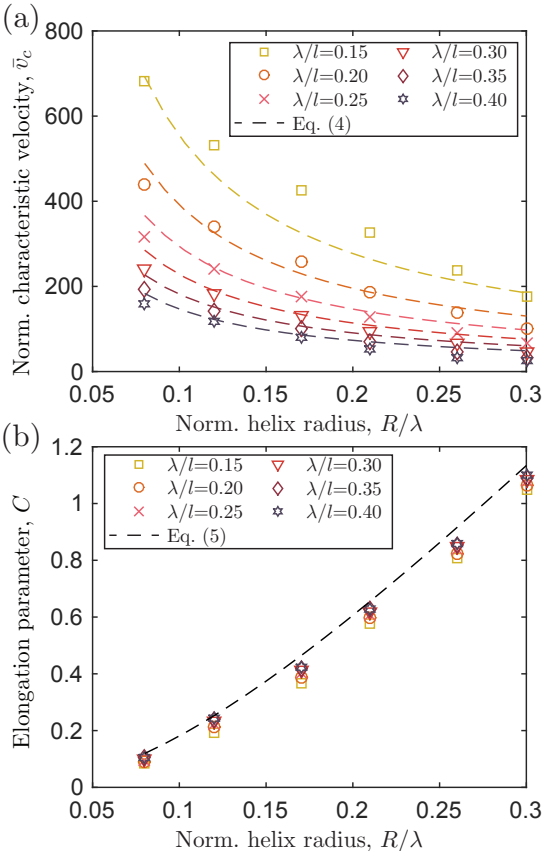


**Fig. 5** (a) Normalized characteristic speed, $\bar{v}_c$ as a function of normalized helix radius, $R/\lambda$, at different values of normalized pitch, $\lambda/l$ (see legend). The dashed lines are fits of Eq. ( 4) to the data with $C_g = 9.78 \pm 0.30$. (b) Dependence of the elongation parameter, $C$, on the normalized helix radius, $R/\lambda$, for different values of $\lambda/l$ (see legend). The dashed line is the prediction from Eq. (5).

For a fixed geometry of the filament, the variation of $C$ on $EI/[\mu l^3]$ is negligible, with a standard deviation that is less than 1% with respect to its mean value $\langle C \rangle = 1.07$ (horizontal solid line in Fig. 4b). This finding further supports our nondimensionalization procedure.

We proceed by describing the dependence of the characteristic speed, $\bar{v}_c$, and the elongation parameter, $C$, on the geometric parameters of the helix. Since a closed form solution is out of reach for us, we perform a numerical survey where we individually vary the normalized pitch, $\lambda/l$, and normalized helix radius, $R/\lambda$, while keeping the remaining parameters fixed at the values of our representative case (except with an increased axial length, $l = 0.4\,\mathrm{m}$, to ensure that the cross-sectional radius is always negligible compared to $\lambda$ and $R$). The results of this parameter sweep are plotted in Fig. 5a where we find that the heuristic form

$$\bar{v}_c = C_g \left( l/R - \lambda/R \right), \tag{4}$$

provides a good description of the data, with $C_g$ as a fitting parameter. The dashed lines in Fig. 5a represent the fits of the experimental curves with different values of $\lambda/l$ to Eq. (4), from which we obtain $C_g = 9.78 \pm 0.30$.

To describe the dependence of the elongation parameter on the geometry of the rod, we evaluate $C$ during the parameter sweep described above, and in Fig. 5b, plot it as a function of $R/\lambda$, for different values of $\lambda/l$. Since the originally helical rod is stretched and becomes approximately straight for axial flows with $\bar{v}_c \gg 1$, the suspended height asymptotes to its contour length, $L = l/\cos(2\pi R/\lambda)$. From this, and without any fitting parameters, we can estimate

$$C = \cos\left(\frac{2\pi R}{\lambda}\right)^{-1} - 1, \tag{5}$$

which is plotted as a dashed line in Fig. 5b. Eq. ( 5) is found to be in good agreement with the simulation data. There is, however, a slight overestimation due to the fact that for $\bar{v} \gg \bar{v}_c$ there is still a small boundary layer region with a curved configuration near the tip and the rod never stretches to be perfectly straight.

Thus far, we have quantified the extension of a non-rotating soft filament subjected to axial flow, and provided a heuristic description of the deformation process, in dimensionless form, as a function of a wide range of the geometric and physical parameters. Combined, Eqs. (2), (4) and (5) allow us to predict the deformation of the helical filament under axial flow, including in

regimes that are relevant for bacterial flagella.

## 5 Rotating filament under axial flow

Natural flagella rotate about their helical axis, simultaneously to the translation (swimming) motion of the bacterium. For the remainder of our study, we address the combined effect of rotation and translation on the deformation of a single helical filament.

It is known that a rotating helical rod fixed in space ($\bar{v}=0$) generates a propulsive force, $F_p$, and undergoes a buckling instability when a critical angular velocity, $\omega_b$, is reached [14,23]. In a previous study [14], we have shown that $\omega_b$ scales with the characteristic frequency, $EI/[\mu l^4]$, as mentioned in §2, and can be nondimensionalized to introduce the dimensionless critical angular velocity, $\bar{\omega}_b = \hat{\omega}_b \omega_b \mu l^4/[EI]$, where $\hat{\omega}_b$ is a numerical prefactor that depends on geometry alone. We have also shown that the propulsive force drops past $\bar{\omega} > \bar{\omega}_b$, and thus $\bar{\omega}_b$ sets an upper bound on the maximum possible propulsion attainable by a helical filament. We now augment these previous findings to also consider the effect of translation at a prescribed axial speed, $v$, in addition to the rotation of the helical filament at a prescribed angular velocity, $\omega$. Our goal is to explore and rationalize the combined effect of $v$ and $\omega$ on the onset of buckling of helical filament, as well as the maximum propulsive force that can be attained.

In Fig. 6a, we plot the normalized height, $\bar{h}$, as a function of $\bar{\omega}$ for a helical rod (with the geometric and physical parameters of the representative case, see §2) in an axial flow with $\bar{v}=1.05$. At $\bar{\omega}_b \approx 225$, the suspended height drops sharply to $\bar{h} \approx 0.5$ when buckling occurs. Typical shapes of the deformed helix prior to buckling ($\bar{\omega}=132$) and after buckling ($\bar{\omega}_b \approx 225$) are shown as insets in Fig. 6a. The corresponding dimensionless propulsive force, $\bar{F}_p = F_p/[EI/l^2]$, normalized by the characteristic bending force, is presented in Fig. 6b as a function of $\bar{\omega}$. The propulsive force is negative up to $\bar{\omega}^* \approx 100$, indicating that the axial flow ($\bar{v}=1.05$) dominates in this regime. In the intermediate regime $\bar{\omega}^* < \bar{\omega} < \bar{\omega}_b$, the propulsive force is positive. For microorganisms, this surplus force would translate into locomotion of the cell body. Buckling occurs at $\bar{\omega}_b$, and, as a result, the propulsive force drops dramatically and becomes unsteady beyond this critical rotation velocity [14]. The oscillations of the $F_p$ signal in the post-buckling regime are due to the complex configurational changes of the deformed filament, a detailed description of which is beyond the scope of this study. The maximum propulsion, $F_M$, that can be generated at a given $v$ occurs immediately prior to $\bar{\omega} = \bar{\omega}_b$. The normalized maximum propulsive force, $\bar{F}_M = F_M l^2/[EI]$, is indicated in Fig. 6b by a star.

As a summary of the findings thus far, our results suggest that, for a given geometry of the helical filament (*i.e.*, $R/\lambda$ and $\lambda/l$) and axial flow velocity, $v$, successful propulsion requires the following two conditions on the angular velocity: (i) $\omega > \omega^*$ such that the propulsion is high enough to overcome the drag from the translational motion and $\bar{F}_p$ is positive, and (ii) $\omega < \omega_b$ to ensure that the hydrodynamic loading does not lead to buckling of the filament.

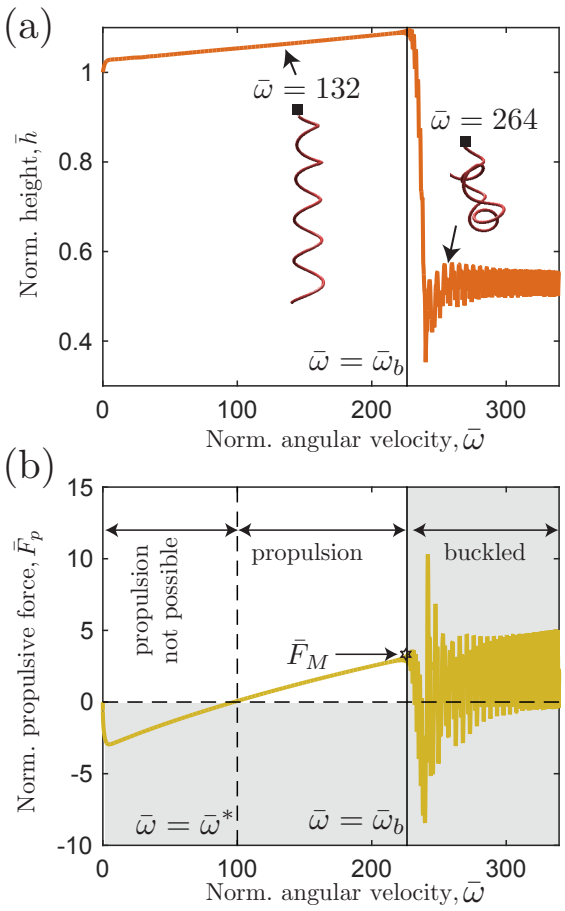


**Fig. 6** (a) Normalized height, $\bar{h}$ as a function of angular velocity, $\omega$ for a helical rod with the physical and geometric parameters of the representative case (see §2), with a fixed axial flow speed of $\bar{v}=1.05$. Buckling occurs at $\bar{\omega} = \bar{\omega}_v$ (b) Normalized propulsive force, $\bar{F}_p = F_p l^2/[EI]$, as a function of $\omega$, with the same parameters as in (a). The vertical dashed and solid lines correspond, respectively, to the lower limit ($\omega = \omega^*$) and upper limit ($\omega = \omega_b$) of the angular velocity for feasible propulsion. The point marked with a star, corresponds to the maximum propulsive force, $\bar{F}_M$, immediately prior to buckling at $\omega_b$

## 6 Biological implications

We now frame the results presented above to the context of bacterial locomotion, in particular regarding the limits of successful propulsion. We consider a series of helical filaments with geometries that were inspired by and taken to be similar to naturally occurring bacterial flagella, the details of which are provided in Table 1.

**Table 1 Geometric parameters of model helices.**

| Model flagellum | $R/\lambda$ | $\lambda/l$ | Bacterium [12,24] |
|---|---|---|---|
| 1 | 0.12 | 0.17 | *Caulobacter crescentus* (Wild) |
| 2 | 0.11 | 0.20 | *Rhizobium lupini* (Curly) |
| 3 | 0.19 | 0.25 | *Rhizobium lupini* (Normal) |
| 4 | 0.09 | 0.36 | *Escherichia coli* (CCW) |
| 5 | 0.09 | 0.37 | *Escherichia coli* (stopped) |
| 6 | 0.09 | 0.25 | *Salmonella* (Wild) |

Making use of our computer simulations, we systematically analyzed the combined rotating and translating motion for these model filaments. We first identified the angular buckling velocity for the non-translating case, $\bar{\omega}_b(0)$, and then calculated the relative shift in buckling, defined as $\Delta_\omega = [\bar{\omega}_b(v) - \bar{\omega}_b(0)]/[\bar{\omega}_b(0)]$, as a function of the dimensionless axial flow speed, $\bar{v}$. The results are plotted in Fig. 7a, where we find that the critical angular velocity at which buckling occurs can be increased significantly (*i.e.*, the onset of buckling can be delayed) as $\bar{v}$ is increased, across all of the configurations. For example, $\Delta_\omega \approx 1$ for $\bar{v} \sim 20$, meaning that the critical angular velocity for buckling is increased by up to $\sim 100\%$, with respect to the case when the filament is not translated. On the other hand, a higher $\bar{v}$ is also accompanied with higher value for the propulsive force required to sustain the axial motion. However, increasing $\bar{v}$ also has the effect of increasing $\omega_b$, which makes some room for more propulsive force to be exerted. This results in a delicate interplay between $\bar{v}$ and the maximum propulsive speed that can be attained, which we quantify next for the same model helices under consideration.

In Fig. 7b, we present the variation of the normalized maximum propulsive force, $\bar{F}_M$ (directly associated with $\bar{\omega}_b$), as a function of the normalized axial speed, $\bar{v}$, and find that there is a regime for which $\bar{F}_M$ becomes negative. This implies that no propulsion is possible for this high values of $\bar{v}$ since the helical filament buckles due to the build up of viscous loading even before the net propulsion is positive. For the filament geometries that we have studied, this threshold occurs approximately within the range $15 \lesssim \bar{v} \lesssim 30$. Therefore, the buckling instability sets an upper limit on the axial speed of the flexible helices. In other words, for a given filament with prescribed material, geometric and fluid parameters, there is a maximum translation speed above which the generation of a propulsive force is unfeasible, at any angular velocity.

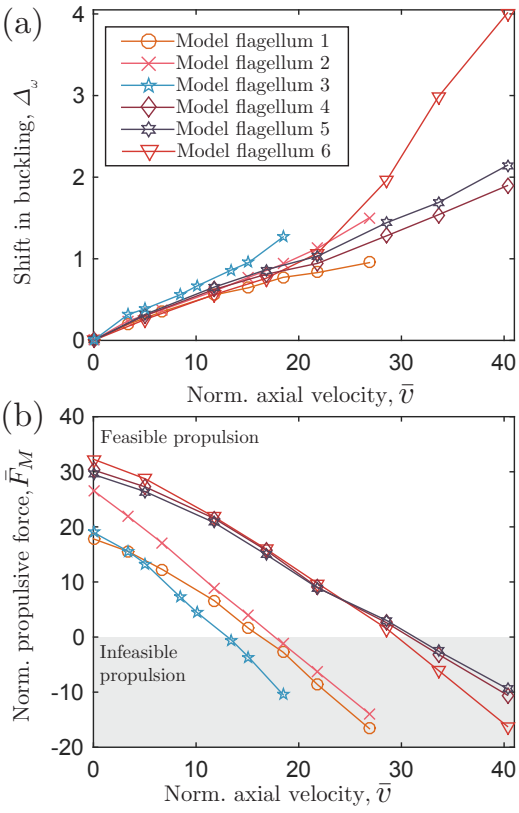


**Fig. 7** (a) Relative shift in buckling, $\Delta_\omega$, as a function of normalized axial velocity, $\bar{v}$, for the different values of $\{R/\lambda, \lambda/l\}$, specified in Table 1. The geometric parameters of our model helices, were inspired by results in the literature [12,24], for some well-known natural bacterial flagella. (b) Dependence of the normalized maximum propulsive force, $\bar{F}_M$, with $\bar{v}$. Similarly to Fig. 5, the material and fluid parameters correspond to the representative case, however, with $l = 0.4$m to ensure that $r_0 \ll \lambda, R$.

In order to relate our findings with bacterial locomotion, we consider the order of magnitude estimates obtained from the literature — ($\mu = 10^{-3}$ Pa.s), ($EI = 10^{-23}$ Nm$^2$) [22], ($v = 20\,\mu$ m/s) [3,24], and ($l = 10\,\mu$ m) — and obtain $\bar{v} = 2$. Note that the estimates for $EI$ reported in the literature [6,25] range from $10^{-24}$ Nm$^2$ to $10^{-22}$ Nm$^2$, which lead to the bounds $0.2 < \bar{v} < 20$. This estimated range does for the most part fall below the threshold axial speed identified above from our simulations ($\bar{v} \approx 15 \sim 30$, see Fig. 7b), which, despite the lack of existing high quality experimental data for $EI$ for a more accurate comparison, is consistent with our analysis. Furthermore, using biological parameters, the angular buckling velocity for the non-translating case for our model flagella lie in the range $2 \cdot 10^2 \lesssim \omega_b(0) \lesssim 2 \cdot 10^3$ Hz, which is comparable to the rotation rate of natural flagella [3,24]. It is important that for some species (e.g. *E. Coli* and *Salmonella*), a more direct comparison to the natural system would require for the interaction between multiple flagella to be taken into account, which is not considered in our analysis.

## 7 Conclusion

We have described and quantified the deformation of a soft helical filament that is simultaneously rotated and loaded by a uniform axial flow at low Reynolds number. Computer simulations were performed to systematically explore the parameter space of the system. Our framework could potentially be used to assist in experimental measurements of the mechanical moduli of bacterial flagella by quantifying the elongation of the filament under prescribed flow conditions and comparing the measured characteristic flow speed, $v_c$, against our predictions. Our study also highlights the fact that, even in the absence of active polymorphism [7], an initially helical rod can dramatically change its shape under an imposed axial flow. Moreover, for a given axial flow speed, we uncovered lower and upper bounds on the angular rotation speed for successful locomotion. For high enough values of the axial flow speed, these two limits can coalesce such that locomotion is no longer feasible, regardless of the angular rotation speed.

We considered specific geometries that were motivated by natural bacterial flagella, and quantified the characteristics of propulsion, as well as the conditions for instability. For simplicity and specificity, we focused exclusively on single helical filaments as reduced model systems for flagella. Future studies should also include the coupling with the hydrodynamics of the cell body, which, combined with our framework, should provide a more detailed model for a self-propelling uni-flagellated bacterium. Moreover, given our implementation of non-local hydrodynamics through Lighthill Slender Body Theory, the case of multiple

helices could also be considered to model the propulsion of multi-flagellated bacteria, *e.g. E. coli* and *Salmonella*. For this purpose, the flexibility of the DER framework can be further augmented to add relevant ingredients, such as self-contact and hydrodynamic interaction with cell body. Beyond a first step towards a better understanding of the role of flexibility in the propulsion of bacteria flagella, our findings may also be used as design guidelines for artificial flagella[26], and provide enhanced understanding to port learning from nature into biomimetic engineering systems.

## 8 Acknowledgment

Our interest in this problem stems from initial discussions with J. Pham, A. Crosby, A. Lindner and O. du Roure. We are grateful for financial support from the National Science Foundation (CMMI-1129894).

## References

1 E. Lauga and T. R. Powers, *Rep. Prog. Phys.*, 2009, **72**, 096601.
2 L. Turner, W. S. Ryu and H. C. Berg, *J. Bacteriol.*, 2000, **182**, 2793–2801.
3 K. Son, J. S. Guasto and R. Stocker, *Nat. Phys.*, 2013, **9**, 494–498.
4 R. M. Macnab and M. K. Ornston, *J. Mol. Biol.*, 1977, **112**, 1–30.
5 M. T. Brown, B. C. Steel, C. Silvestrin, D. A. Wilkinson, N. J. Delalez, C. N. Lumb, B. Obara, J. P. Armitage and R. M. Berry, *J. Bacteriol.*, 2012, **194**, 3495–3501.
6 H. Hoshikawa and R. Kamiya, *Biophys. Chem.*, 1985, **22**, 159–166.
7 N. C. Darnton and H. C. Berg, *Biophys. J.*, 2007, **92**, 2230–2236.
8 R. Vogel and H. Stark, *Eur. Phys. J. E*, 2010, **33**, 259–271.
9 M. Kim and T. R. Powers, *Phys. Rev. E*, 2005, **71**, 021914.
10 J. Lighthill, *SIAM Rev.*, 1976, **18**, 161–230.
11 J. Gray and G. Hancock, *J. Exp. Biol.*, 1955, **32**, 802–814.
12 B. Rodenborn, C.-H. Chen, H. L. Swinney, B. Liu and H. Zhang, *Proc. Natl. Acad. Sci.*, 2013, **110**, E338–E347.
13 J. T. Pham, A. Morozov, A. J. Crosby, A. Lindner and O. du Roure, *Phys. Rev. E*, 2015, **92**, 011004.
14 M. K. Jawed, N. K. Khouri, F. Da, E. Grinspun and P. M. Reis, *Phys. Rev. Lett.*, 2015.
15 M. Bergou, M. Wardetzky, S. Robinson, B. Audoly and E. Grinspun, *ACM Trans Graph*, 2008, **27**, 63.
16 M. Bergou, B. Audoly, E. Vouga, M. Wardetzky and E. Grinspun, *ACM Trans Graph*, 2010, **29**, 116.
17 Numerical simulation source code available at `http://www.cs.columbia.edu/cg/elastic_coiling/`.
18 M. Fujii, S. Shibata and S.-I. Aizawa, *J. Mol. Biol.*, 2008, **379**, 273–283.
19 M. K. Jawed, F. Da, J. Joo, E. Grinspun and P. M. Reis, *Proc. Natl. Acad. Sci.*, 2014, **111**, 14663–14668.
20 G. Kirchhoff, *J. Reine Angew Math*, 1859, **56**, 285–313.
21 J. Miller, A. Lazarus, B. Audoly and P. Reis, *Phys. Rev. Lett.*, 2014, **112**, 068103.
22 Y. Takano, K. Yoshida, S. Kudo, M. Nishitoba and Y. Magariyama, *JSME Int J., Ser. C*, 2003, **46**, 1241–1247.
23 R. Vogel and H. Stark, *Eur. Phys. J. E*, 2012, **35**, 1–15.
24 S. Chattopadhyay and X.-L. Wu, *Biophys. J.*, 2009, **96**, 2023–2028.
25 S. Fujime, M. Maruyama and S. Asakura, *J. Mol. Biol.*, 1972, **68**, 347–359.
26 L. Zhang, J. J. Abbott, L. Dong, B. E. Kratochvil, D. Bell and B. J. Nelson, *Appl. Phys. Lett.*, 2009, **94**, 064107.